



This is a repository copy of *Hyperspectral mapping of human primary and stem cells at cell–matrix interfaces*.

White Rose Research Online URL for this paper:

<https://eprints.whiterose.ac.uk/209672/>

Version: Accepted Version

Article:

De Santis, E. orcid.org/0000-0002-0943-6586, Faruqui, N., Russell, C.T. et al. (11 more authors) (2024) Hyperspectral mapping of human primary and stem cells at cell–matrix interfaces. *ACS Applied Materials & Interfaces*, 16 (2). pp. 2154-2165. ISSN 1944-8244

<https://doi.org/10.1021/acsami.3c17113>

© 2024 The Authors. Except as otherwise noted, this author-accepted version of a journal article published in *ACS Applied Materials and Interfaces* is made available via the University of Sheffield Research Publications and Copyright Policy under the terms of the Creative Commons Attribution 4.0 International License (CC-BY 4.0), which permits unrestricted use, distribution and reproduction in any medium, provided the original work is properly cited. To view a copy of this licence, visit <http://creativecommons.org/licenses/by/4.0/>

Reuse

This article is distributed under the terms of the Creative Commons Attribution (CC BY) licence. This licence allows you to distribute, remix, tweak, and build upon the work, even commercially, as long as you credit the authors for the original work. More information and the full terms of the licence here:

<https://creativecommons.org/licenses/>

Takedown

If you consider content in White Rose Research Online to be in breach of UK law, please notify us by emailing eprints@whiterose.ac.uk including the URL of the record and the reason for the withdrawal request.



eprints@whiterose.ac.uk
<https://eprints.whiterose.ac.uk/>

Hyperspectral mapping of human primary and stem cells at cell-matrix interfaces

*Emiliana De Santis,¹ Nilofar Faruqi,¹ Craig T Russell,² James E Noble,¹ Ibolya E Kepiro,¹
Katharine Hammond,¹ Maria Tsalenchuk,³ Eugeni M Ryadnov,⁴ Magda Wolna,⁵ Mark D Frogley,⁵
Christopher J Price,⁶ Ivana Barbaric,⁶ Gianfelice Cinque⁵ and Maxim G Ryadnov^{1,7, *}*

¹National Physical Laboratory, Hampton Road, Teddington, TW11 0LW, UK

²EMBL-EBI, Wellcome Genome Campus, Hinxton, Cambridgeshire, CB10 1SD, UK

³UK Dementia Research Institute, Imperial College London, London, W12 0BZ, UK

⁴Institute of Neurology, University College London, Queen Square, London, WC1N 3BG, UK

⁵Diamond Light Source Ltd, Chilton-Didcot, Oxfordshire, OX11 0DE, UK

⁶School of Biosciences, University of Sheffield, Sheffield, S10 2TN, UK

⁷Department of Physics, King's College London, London, WC2R 2LS, UK

Corresponding author:

Prof Maxim G Ryadnov; National Physical Laboratory,

Hampton Road, Teddington, TW11 0LW, UK

Tel: (+44) 20 89436078; max.ryadnov@npl.co.uk

ABSTRACT: extracellular matrices interface with cells to promote cell growth and tissue development. Given this critical role matrix mimetics are introduced to enable biomedical materials ranging from tissue engineering scaffolds and tumour models to organoids for drug screening and implant surface coatings. Traditional microscopy methods are used to evaluate such materials in their ability to support exploitable cell responses, which are expressed in changes in cell proliferation rates and morphology. However, the physical imaging methods do not capture the chemistry of cells at cell-matrix interfaces. Herein we report hyperspectral imaging to map the chemistry of human primary and embryonic stem cells grown on matrix materials, both native and artificial. We provide the statistical analysis of changes in lipid and protein content of the cells obtained from infra-red spectral maps to conclude matrix morphologies as a major determinant of biochemical cell responses. The study demonstrates an effective methodology for evaluating bespoke matrix materials directly at cell-matrix interfaces.

KEYWORDS: embryonic stem cells, spectral imaging, extracellular matrices, biomaterials, tissue engineering, synchrotron radiation microspectroscopy

1. INTRODUCTION

Cell-matrix interfaces define the success of biomedical applications ranging from tissue engineering, scarring and tumour models to organoids for drug screening.¹⁻³ Cell responses to extracellular matrix (ECM) materials that provide such interfaces constitute performance metrics essential for the commercialisation of novel cell-based products. Cell imaging is a major source of information to evaluate both the materials and interfaces. Up to date, various imaging modalities have been used to characterise the physical behaviour of cells across length scales. Light microscopy helps investigate changes in cell morphology and proliferation,⁴ electron microscopy proves indispensable for elucidating subcellular organisation,⁵ and atomic force microscopy (AFM) provides important insights into cell topography.⁶ However, none of these established approaches can reveal chemical information. To address this shortcoming, analytical methods, which otherwise are developed to assess molecular composition, are being reimagined into imaging capabilities. Mass spectrometry and atom probe tomography, infrared (IR) and Raman spectroscopies become common tools to image cells and their components, prompting the introduction of chemical imaging modalities to assign molecular spectra to

cells in a spatially localised manner.⁷⁻¹⁶ In this endeavour, much interest focuses on the intracellular distribution of drugs and metabolites. Molecules exhibiting chemistries, which are not normally present in cells, e.g., unique atoms such as halogens, are favoured. Since this requirement is not always possible chemical imaging employs labelling strategies, e.g., the use of isotopes.⁷ Irrespective of the approach used, significant progress has been made in generating spectral or chemical maps of individual cells on surfaces and in suspension enriching information content of drug uptake at intracellular interfaces.¹⁷⁻²⁰ By marked contrast, the evaluation of cell responses at extracellular material interfaces remains in infancy.

Connective tissues require ECM substrates, which support cell signalling, growth, and motility. Given the importance of such substrates for tissue formation and repair, a variety of bioinspired ECM mimetics has been developed. Such materials provide physicochemical cues to cell development by interfacing with cell receptors and cytoplasmic projections.²¹ Cells respond with changes in morphology and proliferation rates, which can be monitored using physical imaging modalities. However, the impact of ECM materials on the biochemical composition of cells they interface with has yet to be shown. Here we bridge this gap by generating and cross-comparing IR spectral maps of human primary and stem cells seeded on native and synthetic ECMs.

2. EXPERIMENTAL SECTION

2.1. ECM mimetic materials

ECM mimetics used in the study were prepared as described elsewhere.²²⁻²⁵ Collagen and vitronectin (Invitrogen) and were prepared as per the supplier's protocols.

2.2. SR-IR microspectroscopy

ECM-cell and control samples were imaged at the SR-IR beamline 22 of Diamond Light Source – Multimode InfraRed Imaging And Microspectroscopy (MIRIAM) – using a Hyperion 3000 IR microscope coupled with a Vertex 80V in vacuum interferometers (Bruker UK) to acquire IR maps in scanning mode. Spectral and optical features of the beam can accessed directly from the beamline performance description at: <https://www.diamond.ac.uk/Instruments/Soft-Condensed-Matter/B22/specs.html>, and as described elsewhere.^{26,27} 36x magnification objective/condenser optics either in transmission or transreflectance modes via a high sensitivity MCT detector 50 µm pitch size were

used.²⁶ Routine measurement conditions were 80 kHz scanner acquisition rate, coadding typically 256 scans (equivalent to 35 sec spectral acquisition per point), and microscope slits set to 10-15 μm at the sample plane by view-through slit blades in an outcoming beam path (i.e., quasi-confocal). Spectra were collected using a $10 \times 10 \mu\text{m}^2$ aperture, with a spatial resolution of 4 cm^{-1} . The oversampling of IR mapping was set to ca. 2 times to achieve the best quality of hyperspectral images. Background measurements were taken from Uncoated UV graded CaF_2 slides ($26 \times 22 \times 0.5 \text{ mm}$) (Crystan Ltd, UK). All measurements were conducted in transmission mode.

2.3. Pre-processing

Subsequent processing of FTIR spectra involved several steps, with OPUS software (OPUS 7.8, Bruker Optics) utilized for baseline correction and normalization (Standard Normal Variate – SNV) and smoothing. Spectra were cropped to specific regions of interest, including $2740\text{--}3000 \text{ cm}^{-1}$ (lipid region) and $1510 \text{ cm}^{-1}\text{--}1700 \text{ cm}^{-1}$ (protein region). SNV normalization was applied after baseline correction to eliminate sample thickness effects and baseline offsets.

Principal Component Analysis (PCA) was performed as an unsupervised analysis to reduce the dimensionality of microFTIR spectral vectors. This process generated principal components which were calculated from the covariance of the datasets. PCA identified differences within the data sets, and PC scores were used to plot variance on a 2D axis. The position of the score on the axis represented the relative position of variance compared to other plots of variance.

2.4. Statistical analysis

Statistical analysis was used to compare chemical differences in cells on different substrates. Individual cells in populations of 50-100 cells were imaged and analysed per sample substrate, with each substrate done in triplicate for every condition used. IR signals were correlated using Pearson's correlation and significances and p-values were extracted (<https://docs.scipy.org/doc/scipy/reference/generated/scipy.stats.pearsonr.html>). The Pearson correlation coefficient and *p* values were utilized for testing non-correlation, and the Pearson correlation coefficient was used to gauge linear connections between two datasets. The coefficient, ranging from -1 to +1, denotes the strength of the relationship. Positive values denote corresponding increases, while negative values indicate proportional decreases. All analysis was performed using R Statistical Software

(www.r-project.org). Initial IR signals were subsets to lipid (1700-1500 cm^{-1}) and protein (3000-2800 cm^{-1}) regions. Subsequent sum-normalization was applied to each window. To enhance data quality, aberrant wavelengths were filtered out using the mvOutlier package, while the mdatools package was used to extract the first two principal components, which underwent scaling and centering of the IR windows. The non-linear Iterative partial least squares method, known for its resilience to missing data, was employed for this purpose. IR signal relationships were determined through Pearson's correlation, with significance metrics and p values. Figure 4 visualizes the PCA of the IR spectra, with each cluster's bounding ellipse determined by Hotelling's T^2 . This method, rooted in the chi-square test, delineates the 95% confidence boundary.

2.5. Cell culture and seeding

Human dermal fibroblasts (hDFs) were purchased from Invitrogen. Human embryonic stem cells (hESCs), H7 (WA07) and H14 (WA14) were originally established in the laboratory of James Thomson.²⁸ Early passage sublines of H7 (H7.s14) and H14 (H14.s9) used in this study were established and maintained in the Centre for Stem Cell Biology.²⁹ Cell stocks of both sublines H7.s14 and H14.s9, were characterised as karyotypically normal (based on 30 metaphases analysed by G-banding of cell banks prior to experiments) and did not possess the commonly gained 20q11.21 copy number variant (as determined by Fluorescent In Situ Hybridisation). H7.s14 and H14.s9 cells were used within 20 passages. The hDFs were maintained in Medium 106 supplemented with low serum growth supplement (2% v/v) and antibiotics (10 $\mu\text{g}/\text{mL}$ gentamicin; 0.25 $\mu\text{g}/\text{mL}$ amphotericin B) in 25 cm^2 culture flasks. The medium was then switched to the medium (Medium 106) supplemented with low serum growth supplement (5% v/v) for the long-term evaluations (proliferation).

Human ESCs were cultured on flasks coated with 5 $\mu\text{g}/\text{ml}$ of vitronectin (Life Technologies) diluted in Dulbecco's phosphate buffered saline and maintained in essential 8 medium (Life Technologies). The cells were incubated at 37 $^{\circ}\text{C}$, 5% CO_2 and 95% air humidity. At 70-80% confluency cells were washed with phosphate buffered saline (PBS) to remove the unattached cells and then adhered cells were trypsinized (trypsin/ethylenediaminetetraacetic acid 0.025:0.01%) followed by trypsin neutralizer (all from Invitrogen, UK). The harvested cells were seeded for subsequent cellular analysis. To evaluate initial cell attachment and spreading, well-separated cells (zero cell-cell contact) were seeded on the

glass substrates coated at a low seeding density of 1×10^3 in a serum-free essential 8 medium. For cell attachment (first hours) cells were seeded at a density of 4×10^3 in the serum-free medium on substrates (sterile 96 well plates) coated with 50 μ L of ECM, collagen or vitronectin (0.4-0.5 g/L). The medium was then switched to the medium used supplemented with low serum growth supplement (5% v/v) for the long-term evaluations (proliferation) non-differentiating conditions, and with low serum growth supplement (5% v/v) together with retinoic acid (10 μ M) for differentiating conditions. Conditioned media was prepared using Dulbecco's modified eagle medium + F12 supplemented with serum (10%, v/v), FGF (1:1000 dilution), ROCK kinase inhibitor (Y-27632), with amino acids.

2.6. Cell-matrix samples

All the samples were prepared following our published protocols.²²⁻²⁵ ECMs were assembled overnight in 10 mM phosphate or 3-(N-morpholino) propanesulfonic acid buffers (pH 7.4, 100 μ M total peptide or protein) and then deposited onto CaF₂ windows, which are transparent in the infrared region and were used for SI-IR and AFM. The windows and blotting filter paper were pre-sterilised by UV over 20 min. Similarly, assembled ECMs were deposited (5-10 μ L) on glow discharged (30 sec) Quantifoil R2/2 gold grids (200 mesh) for TEM, pre-sterilised by UV over 20 min. The excess buffer was removed using blotting filter paper, and the substrates were used straight away without drying. Cells were added to the substrates, the cell media was exchanged after 30 min and the cell-matrix substrates were incubated over 24 hours at 37°C (or defined time points if stated otherwise). The media was then removed, the samples were fixed over 30 min using 4% formalin solution in PBS for SR-IR and AFM and over 15 min using 5% glutaraldehyde solution in 10 mM phosphate buffer for TEM, followed by washing (3x) with the buffer, distilled water and drying prior to the analysis. Each sample was prepared in triplicate. ECM substrates without cells were used as blank, control samples. Uncoated CaF₂ substrates were used as negative controls during culturing cells.

The spectra and heatmaps presented are raw data without the removal of the matrix protein content. The subtraction of the matrix contributions (substrates without cells) from the cell spectra was not deemed appropriate, while no differences in SR-IR maps could be ascertained in protein content in samples before and after the subtraction (not shown). Considering the imaging set up, the cells cover the

matrices, making them indistinguishable for imaging, and may produce their own collagen over time increasing protein content.

2.7. Transmission electron and atomic force microscopy

Cell-matrix samples were prepared as above. Staining was performed using phosphotungstic acid (aq. 2%) over 5 min. The excess stain was removed by blotting. Electron micrographs were recorded in a Tecnai T20 twin lens scanning transmission electron microscope (FEI Co.) at 200 kV, using a proprietary FEI Eagle 4k x 4k CCD camera and were analyzed using Fiji analysis software. AFM images (height) were obtained at MIRIAM B22 beamline using a Nanonic Nanonics MV1000 AFM and Au coated silicon cantilever (BudgetSensors).³⁰ AFM images were processed via line-by-line subtraction of first-order fits to the background using Gwyddion.

2.8. Fluorescence imaging

Imaging was performed using fluorescently labelled antibodies (from Abcam and Invitrogen). For (I) in Figures 5C and S5, cells were fixed using 4% paraformaldehyde (PFA) and blocked using 10% FCS in PBS. Anti-SSEA3 IgM antibodies (rat) targeting stage specific embryonic antigen 3 (SSEA3) were then added to the cell samples at 1:10 dilution and the samples were incubated for 1 hr. The cells were washed (4x) with PBS (used in all subsequent washing steps) and secondary antibodies (anti-rat IgM-Dylight-549, 1:100 dilution) were added to the samples followed by the incubation over 1 hr. The cells were then washed (4x), permeabilised using 0.1% Triton X and washed again. Anti-OCT4 monoclonal antibodies (rabbit) were then added at 1:100 dilution and the samples were incubated over 1 hr. The cells were washed (4x) and secondary antibodies (rabbit, anti-IgG) labelled with DyLight™ 488 (anti-rabbit, 1:100 dilution) were added for 1 hr, followed by the addition of Hoechst 33342 at 1:1000 dilution. The cells were washed (4x) and ProLong™ Gold (Thermo Fisher, UK) was added to preserve the fluorescence for imaging using a confocal laser scanning microscope IX81 (Olympus, UK), and an InCell analyzer 1000 (GE Healthcare).

For (II) in Figures 5C and S5, cells were fixed with PFA, blocked with 10% FCS in PBS, permeabilised, washed and stained using Ki67 monoclonal antibodies (rabbit, 1:100 dilution) followed by secondary antibodies labelled with DyLight™ 488 (anti-rabbit, 1:100 dilution), and Hoechst 33342 (1:1000 dilution). The cells were then washed (4x) and ProLong™ Gold (Thermo Fisher, UK) was added to

preserve the fluorescence for imaging using a confocal laser scanning microscope IX81 (Olympus, UK), and an InCell analyzer 1000 (GE Healthcare, UK). For (III) in Figures 5C and S5, cells were fixed with PFA, blocked with 10% FCS in PBS, permeabilised, washed and stained using anti-pFAK phospho-Y397 (rabbit) followed by secondary antibodies labelled with DyLight™ 488 (anti-rabbit, 1:100 dilution) or high affinity F-actin probe (phalloidin B7474), followed by Hoechst 33342 (1:1000 dilution). The cells were then washed (4x) and ProLong™ Gold (Thermo Fisher, UK) was added to preserve the fluorescence for imaging using a confocal laser scanning microscope IX81 (Olympus, UK), and an InCell analyzer 1000 (GE Healthcare, UK).

3. RESULTS AND DISCUSSION

3.1. Experimental design

Changes in the biochemical composition of single cells that can be detected by IR in a given population or between different populations or different cell types may relate to their dynamic heterogeneity or different growth stages, but largely appear to be similar.^{20, 31-33} Partly, this is because spectral data is complex and requires multivariate analysis methods such as the PCA, and partly because same matrix types of same morphologies, typically collagens, are used as substrates for cell attachment and growth, or no substrates used at all, which excluded the impact of matrix interfaces in cell development.^{19,20,31-}
³⁴ Therefore, the aim of this study becomes three-fold. First, it is to obtain hyperspectral IR maps of human primary and stem cells grown on a range of different ECMs. Second, it is to reveal biochemical responses of the cells to these ECMs, focusing on comparative changes in total protein and lipid content in single cells in independent samples of up to 100 cells for each matrix and condition used. Third, it is to statistically cross-compare such responses using the PCA and to reveal probable differences in the responses. To enable this, a principal variation factor in cell-matrix interactions was chosen to be the morphology of the ECMs. Synthetic ECMs of *de novo* design, with varied fibrillar microstructure and composition, were used.²²⁻²⁵ None of these ECMs incorporates known biology, i.e., cell adhesion motifs or receptor ligands, which may otherwise influence cell responses. The results of cross-comparisons are then used to gain insights into the effect of changing biochemical composition on the proliferation of stem cells. Thus, the overall rationale of the study is to understand if the cells change their chemical composition significantly and comparatively in response to different matrix morphologies, if these

changes could be monitored by chemical imaging and how they translate into basic cell functions, such as proliferation.

The study employs IR spectroscopic imaging which allows for correlation between Fourier transform infrared (FTIR) microspectra and optical micrographs to map the biochemical composition of single cells.³³⁻³⁶ Referred to as microspectroscopy, the approach utilises changes in the IR-active vibrational modes of molecules to measure molecular content and spatial distribution across large sample areas at the microscopic scale without labelling.³⁷⁻⁴³ When coupled with synchrotron radiation (SR), this mode of imaging reaches high spatial resolution and high signal-to-noise ratios to enable chemical single-cell analyses.³⁶⁻³⁹

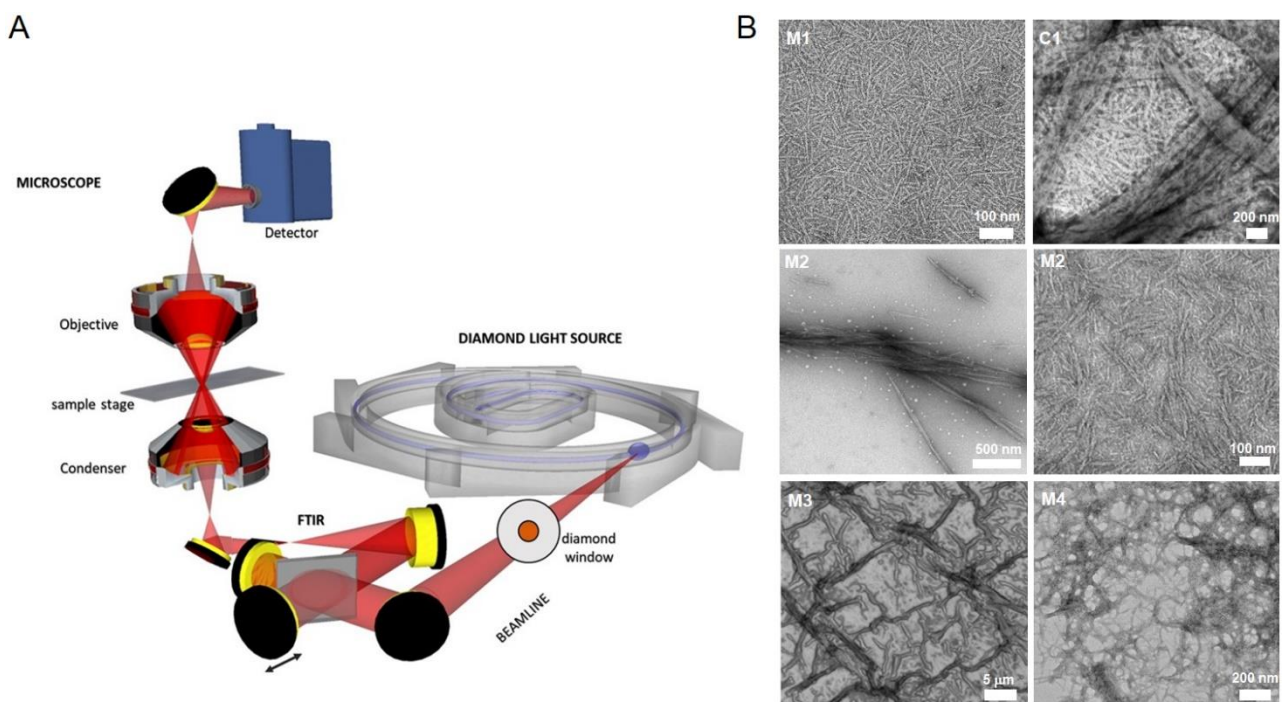


Figure 1. Experimental design. (A) SR-IR microspectroscopy. A schematic representation of IR imaging developed at Diamond Light Source (Beamline B22). Adapted with permission from²⁷ © Optical Society of America. (B) Electron (M1, M2, M4 and C1) and optical (M3) micrographs of the ECM materials used in the study. Two micrographs given for M2 demonstrate the morphological heterogeneity of the material.

In this study, we probe the biochemical responses of hDFs and hESCs to ECM substrates, native and synthetic, using SR-IR microspectroscopy established at Diamond Light Source (beamline B22). Figure 1A shows the SR-IR set up used in the study.

3.2. ECM mimetic materials

ECM mimetics used in the study are nano-to-microscopic fibrous materials self-assembled from *de novo* polypeptide sequences, which are dubbed mimetics 1-4 (M1-M4) (Table 1). Previously we have shown that such mimetics effectively promoted cell proliferation and exhibited bacteriostatic effects thereby supporting differential biological responses.²²⁻²⁵ This study cross-compares compositional changes in cells grown on M1-M4 and on collagen type I (C1), which is a native ECM, and which was used as a control substrate for the study (Table 1, Figure 1B). All these materials, M1-M4 and C1, are fibrous products of protein self-assembly; that is, chemically equivalent, but are different from one another in morphology; that is, physically distinct. We reason here that cells should tailor their biochemical composition in response to matrix morphologies rather than chemistries. To directly probe cell responses at the cell-matrix interfaces without the complexity of bulk properties such as gelation, cell encapsulation and tensile strength, cell attachment experiments were used.

Table 1. ECM materials used in the study.

Name*	primary structure	secondary structure
M1	KIAALKQKIAALKQKIAALKKEIAALEYEIAALEQEIAALEQ	α -helix
M2	KIAALKQKIAALKKEIAALEYEIAALEQ	α -helix
M3	cyclo(EIAALEGGGEIAALEQEIAALEYKIAALKGGGKIAALKQKIAALKQ)	α -helix
M4	C ₁₈ -CGCQLR-am	β -sheet
C1	collagen type I	PPII helix

*M – artificial mimetic matrices, C – native collagen matrix

3.3. IR hyperspectral mapping of human primary cells

All the ECM substrates used supported cell adhesion and proliferation, consistent with previous reports. By contrast, the cells were not viable on uncoated CaF₂ windows used for mounting samples. No cell attachment was observed indicating that the ECM substrates are necessary for cell support. Optical microscopy was used to locate and image cells focusing on the centre and periphery of individual cells (Figures 2A & S1). As gauged by transmission electron microscopy (TEM) and atomic force microscopy (AFM), the cells effectively covered the matrices they were grown upon (Figure S2). Protein content of cells proved to be higher than that in the matrices per unit area. Cells also tend to re-arrange the matrix they grow on and shed their own collagen concentrating at the edges of the cells, which is particularly characteristic of fibroblasts, stromal and stem cells (Figure S2).^{44,45} This was evident by comparing the obtained spectral heatmaps for lipid and protein content. In the same images,

the areas with no cells present (blue) show similar or more content for protein maps when compared to that for lipid maps, but never the other way around (Figures 2A & S1).

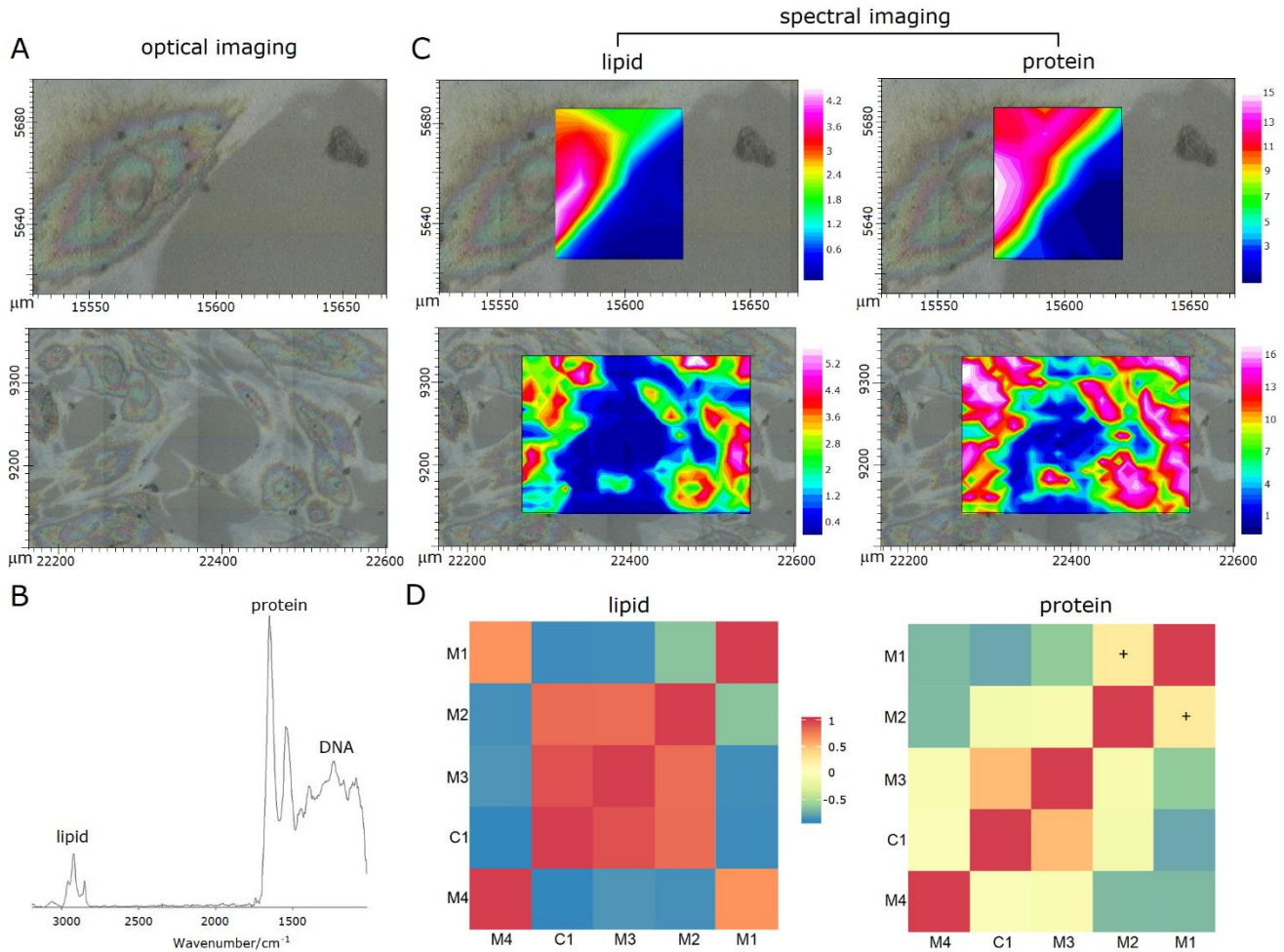


Figure 2. Spectral mapping of human dermal fibroblasts at cell-matrix interfaces. (A) Representative optical micrographs (uncolored) of hDFs, a single cell (upper) and a population (lower), grown over three days on CaF₂ windows coated with M1. (B) A representative FT-IR spectrum of (A, upper). (C) SR-IR maps (colored) of hDFs correlated with and superimposed on the optical micrographs from (A), showing lipid and protein contents. The rainbow scale changes from blue (no content) to white (saturated content). Numerical values refer to the integrated absorption band as relative, arbitrary units, and within the spatial coordinates of the optical micrographs. (D) Spectral heat maps showing correlations in lipid and protein contents for hDFs seeded on different matrices. The rainbow scale represents the Pearson correlation co-efficient and changes from blue (negative correlation) to red (strong positive correlation). Yellow pixels indicating slight positive and negative correlations closed to zero are labelled "+" and "-" in the heatmaps to distinguish them from zero pixels which remained unlabelled.

FT-IR spectra revealed fingerprint bands for lipids, O-H, N-H and C-H stretching at 3050-2800 cm⁻¹, and proteins, C=O stretching (amide I), N-H bending (amide II) at 1700-1100 cm⁻¹. Specific bands could

be identified for methyl-methylene groups of aliphatic regions in lipids and proteins (1454 cm^{-1}), COO-stretching vibrations of amino-acid chains (1396 cm^{-1}), P=O asymmetrical and symmetrical stretching vibrations for phosphodiester groups (1238 cm^{-1} and 1080 cm^{-1}), C-O stretching vibrations coupled with C-O bending of the C-OH groups of carbohydrates (1030 cm^{-1}), ribose phosphates ($986\text{--}992\text{ cm}^{-1}$), and the stretching vibration of DNA backbone (966 cm^{-1}) (Figure 2B).

For all the matrices, the lipid content, as gauged by the integration of CH₂ and CH₃ stretching vibrations ($2970\text{--}2840\text{ cm}^{-1}$), was smaller and more localised than the protein content characterised by amide I and II bands ($1510\text{--}1700\text{ cm}^{-1}$) (Figure 2B). Consistent with earlier observations,³⁶ the lipid content was more appreciable in perinuclear regions suggesting the presence of lipid-rich organelles, e.g., the endoplasmic reticulum (Figure 2C). Lower, but apparent lipid signals in the periphery of the cell may be attributed to other lipid-rich organelles, e.g., mitochondria. According to the principal component analysis (PCA), no statistically significant differences in lipid content could be ascertained for the cells seeded on M2, M3 and C1 (Figure 2D). Significant differences were found between these three matrices and M1 and M4, but not between M1 and M4. This is intriguing as M1 and M2 have the same amino-acid compositions, and are chemically identical to M3, while M4 is the only matrix incorporating a lipid group in its primary structure (Table 1). The differences observed in the lipid content are likely to relate to differences in matrix morphologies. Indeed, M1 and M4 tend to form denser, carpet-like matrices of smaller and thinner fibres, whereas M2, M3 and C1 are more heterogeneous materials comprising thicker fibres that can extend microns in length. By comparison, the protein content of the cells varied more significantly between the matrices (Figure 2D). Statistically notable differences were observed between M1 and the other matrices, except between M1 and M2. Less significant positive correlations were observed between these matrices. Cells on M2, M3, M4 and C1 proved to give statistically comparable levels of protein content, with no correlations observed. Negative correlations between cells grown on M2 and M4 provided an exception, and were more significant. In contrast to all, C1 and M3, which are morphologically similar matrices, showed significant positive correlations in the protein content with the same directionality of variance, indicating that cell responses to these matrices were significantly different from those to the other matrices, but the responses between C1 and M3 were not. This is consistent with cell responses reported previously for C1 and M3, which featured comparable

proliferation rates and enhanced filopodia expressions.^{23, 46} In addition, the two matrices span same microscopic length scales by forming polygonal networks of extended and thickened fibres. M4 also forms polygonal networks, albeit of shorter fibres, which might explain the lack of statistical differences in protein content between cells on this matrix and those on M3 and C1. It also appeared that M1 and M2 fibres, which do not network, promote somewhat different levels of protein expression in cells they support. At least partly, this can be explained by that cells cultured on M1 had twice the proliferation rate of the cells grown on M2.²⁴ No statistically significant differences were found between M2 and M3 and M2 and C1, as opposed to significant differences between M1 and M3 or C1. This may reflect similarly heterogenous compositions of thicker fibres in M2, M3 and C1 – a trend that mirrors that observed for the lipid content (Figure 2D).

Collectively, the findings indicate that the chemistry of the matrices does not impact significantly on cell responses as judged by changes in protein and lipid contents. Differences in the folding characteristics of the matrices did not appear to give clear correlations either. Indeed, cell responses to M1-M3, which are all α -helical by nature, were not identical. Similarly, C1, M4 and M3 which adopt polyproline helix type II, β -sheet and α -helix conformations, respectively, gave statistically significant differences in the lipid content, but not in the protein content.

The analysis revealed that the distinct morphologies of the matrices determine changes in the biochemical composition of individual cells. Differences in the lipid content were less profound than those in the protein content, suggesting that lipid synthesis is not impacted by cell-matrix interactions to the same extent as the total protein. Given that there is four times more protein than lipid in the cell, statistically more significant differences observed in the protein content are striking and indicate differential cell responses to distinct matrix morphologies.

3.4. IR spectral mapping of human embryonic stem cells

The ECM materials used in this study do not incorporate specialist biology, e.g., known cell adhesion motifs. The cell responses observed to these matrices appear as predominantly driven by differences in matrix morphologies. The collagen matrix C1, which exhibits both fibrous morphology and endogenous biology (i.e., cell adhesion motifs) provides an exception in this regard. Biology contributions such as these are not critical for primary, differentiated cells but may impact on the growth of non-differentiated

cells.⁴⁷⁻⁴⁹ To help delineate biology contributions from those of matrix morphologies requires an additional control coating: a non-fibrous, matrix protein that is able to support stem cell growth and proliferation. Unlike the ECMs, V does not assemble, is non-fibrous, but is protein-based, i.e., chemically similar to the substrates, and is a native matrix protein, i.e., biologically intrinsic to support stem cell differentiation. Unlike hDFs, hESCs are strongly dependent on adhesion to matrix proteins, in particular vitronectin, which guides their differentiation.⁴⁷ With this in mind, we performed the same analysis for hESCs under the same (non-differentiating) conditions using C1, as the fibrous native ECM, M1 and M3, which were chosen to represent two most distinct morphologies of the ECM mimetics, and vitronectin (V). Similar to hDFs, hESCs could only attach to coated CaF₂ windows (Figure 3A).

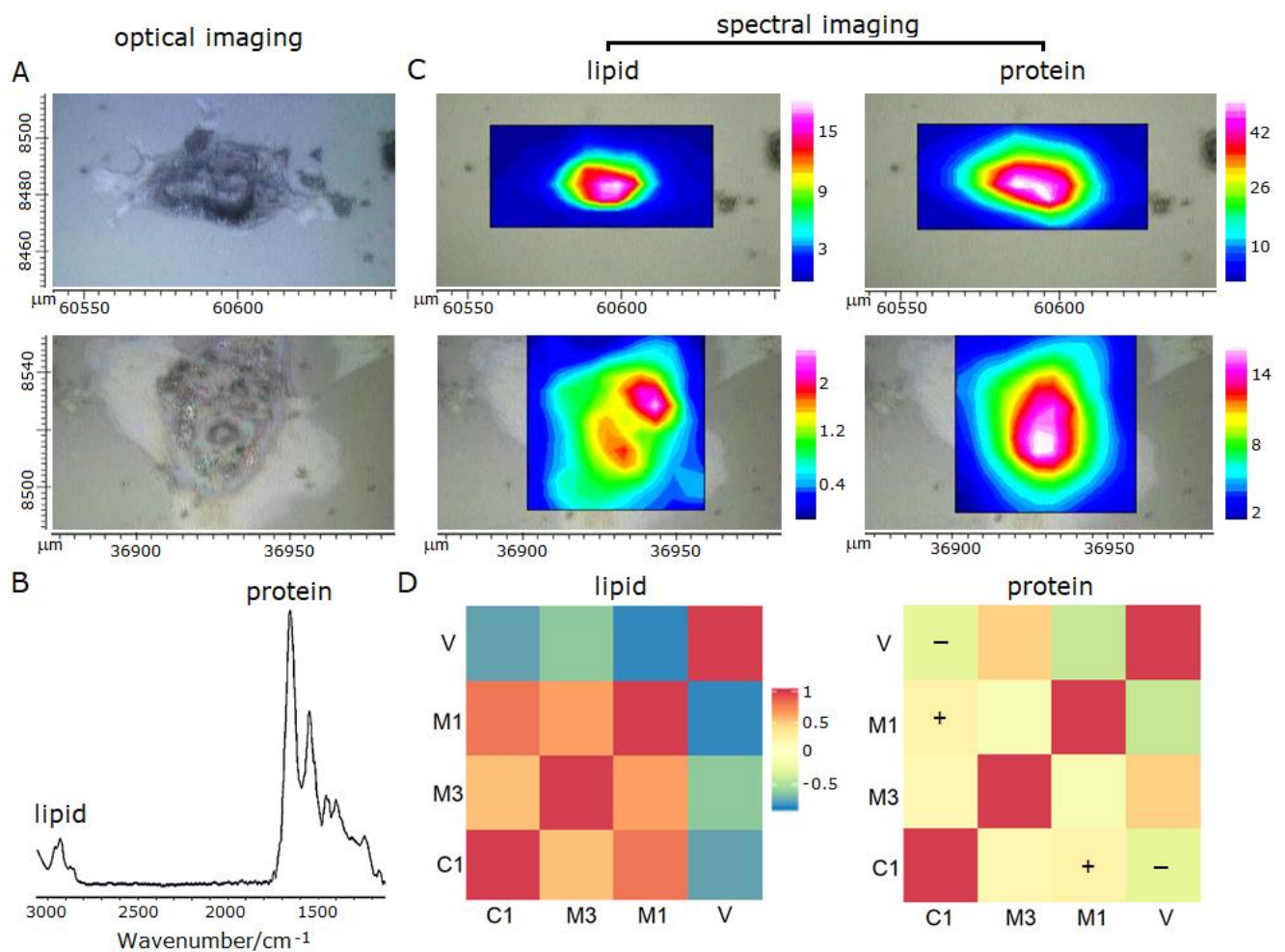


Figure 3. Spectral mapping of human embryonic stem cells at cell-matrix interfaces. (A) Representative optical micrographs (uncolored) of hESCs grown under non-differentiating conditions over three days on CaF₂ windows coated with M3 (upper) and vitronectin (lower). (B) A representative FT-IR spectrum of (A, upper). (C) SR-IR maps (colored) of hESCs correlated with and superimposed on the optical micrographs from (A), showing lipid and protein contents. The rainbow scale changes from blue (no content) to white (saturated content). Numerical values refer to the integrated absorption band as relative, arbitrary units, and within the

spatial coordinates of the optical micrographs. (D) Spectral heat maps showing correlations in lipid and protein contents for hESCs seeded on different matrices. The rainbow scale represents the Pearson correlation coefficient and changes from blue (negative correlation) to red (strong positive correlation). Yellow pixels indicating slight positive and negative correlations closed to zero are labelled “+” and “-“ in the heatmaps to distinguish them from zero pixels which remained unlabelled.

FTIR spectra of the attached cells revealed the characteristic bands of lipid and protein (Figures 3B & S3A). As expected, SR-IR maps indicated more protein than lipid in individual cells (Figure 3C). No statistically significant differences in the lipid content were observed between hESCs grown on all the ECM materials tested, but for all the content was statistically different from that for hESCs grown on V (Figure 3D). This is in contrast to hDFs for which significant differences in the lipid content were found between M1 and M3, M1 and C1 (Figure 2D). Unlike for hDFs, no statistically significant differences were found in the protein content for hESCs grown in all the coatings tested (Figure 3D). Such marked differences between hDFs and hESCs in responses to the matrices, in particular to M1, M3 and C1, prompted a cross-comparison analysis between these cells on the same matrices (Figures 4 & S3B).

By comparison, most significant differences between hDFs and hESCs were in the protein content for M3, with most discriminating wavelengths corresponding to amide I regions in the spectra (Figures 4B & S3B). PCA plots for M3 showed no significant overlaps between cluster bounding ellipses, but clear separation within the negative and positive variability ranges (Figure 4A). For M1 some separation between clusters could be ascertained, but strong overlaps were evident, whereas no differences could be drawn with confidence for C1. For the lipid content, cluster overlaps for C1 and M1 were most significant, indicating that differences in responses between the cells grown on these matrices were not significant. C1 gave a relatively more spread cluster for hDFs, which may indicate that cell responses were different from those of hESCs. However, the overlaps between the two cell types were most significant for C1, whilst the spread appeared to be non-discriminating between positive or negative values of the PCA plots (Figure 4A).

All three matrices are morphologically different (Figure 1B), while M1 and M3 are chemically equivalent (Table 1). Since for hESCs the most significant differences, among all the matrices, were found between M3 and V (Figure 3D), the cells grown on M3 and V under differentiating conditions were tested.

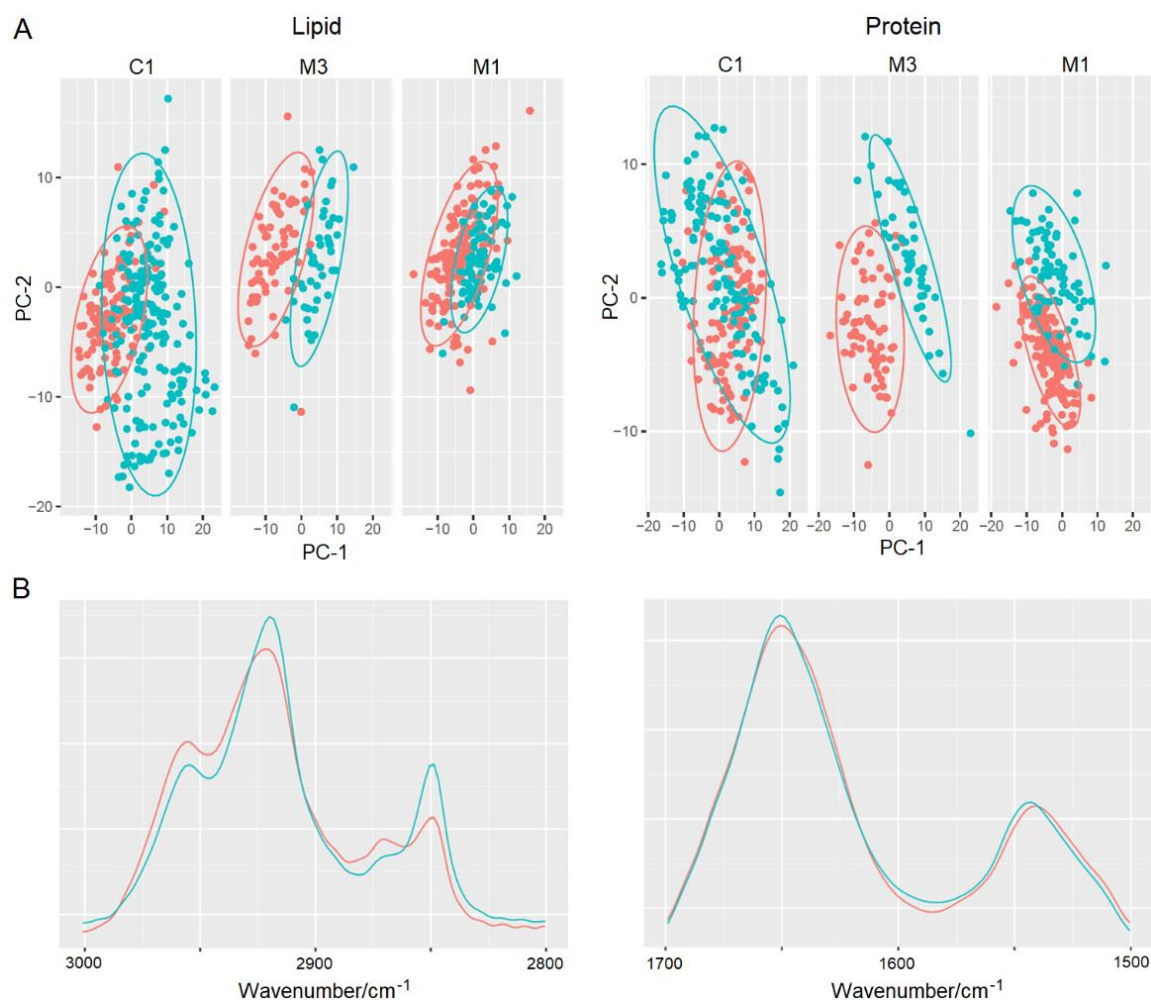


Figure 4. Cross-comparison of human primary and embryonic stem cells at cell-matrix interfaces. (A) PCA plots for hDFs (cyan) and hESCs (orange) grown on the matrix materials over three days. (B) Representative FT-IR spectra of lipid and protein regions for hDFs (cyan) and hESCs (orange).

SR-IR maps of the cells grown on M3 and analysed at different time points shared no statistically significant differences, with individual scores in the PCA clustered together (Figure 5A, B). PCA loading plots, used to identify IR regions contributing to the clustering, revealed that most variables were in the spectral regions corresponding to lipid and protein contents. Comparatively more significant changes appeared in the lipid content. The wavenumbers varied beyond the ranges of ≥ 0.1 and ≤ -0.1 , indicating significant variations. Values in the PC1 loading reflect the expected fingerprint signals of C-H stretching, CH₃ and H-CO. The wavenumbers for the protein content remained largely within the loading plot ranges (Figure 5B). In contrast, significant variations were observed in the biochemical composition of the cells grown on V at different time points, which was evident in both score and loading plots. As was the case for M3, the loading plots showed that changes in the lipid and protein regions contributed most to the clustering observed in score plots. High positive values in the protein

region were predominantly for amide I and II bands suggesting that α -helix and β -sheet structures contributed most of the discriminating wavenumbers for the protein content. Variations in the lipid content were similarly high for V.

This distinction suggests that cell responses on M3 are complete on day 1 without significant changes in the biochemical composition over time. Further support for this came from cross-comparisons performed under both conditions. These showed that differences between M3 and V were statistically significant for cells grown under non-differentiating conditions, but not under differentiating conditions (Figures 5A, B & S3C). Variations in clustering for non-differentiating conditions could be observed, but the differences remained statistically significant. Interestingly, contributions from the protein content were more discriminating than those for the lipid content for both the differences under non-differentiating conditions and the differences between differentiating and non-differentiating conditions (Figures 5 A, B & S3C). In all cases higher values were detected for wavenumbers corresponding to amide I bands indicating larger contributions from α -helical structures, likely actin filaments. These values may also include contributions from cellular collagen. However, amide II (e.g., 1550 cm^{-1}) and amide III (e.g., 1240 cm^{-1}) wavenumbers that typically accompany amide I bands for collagen did not discriminate significantly (Figure 5B).

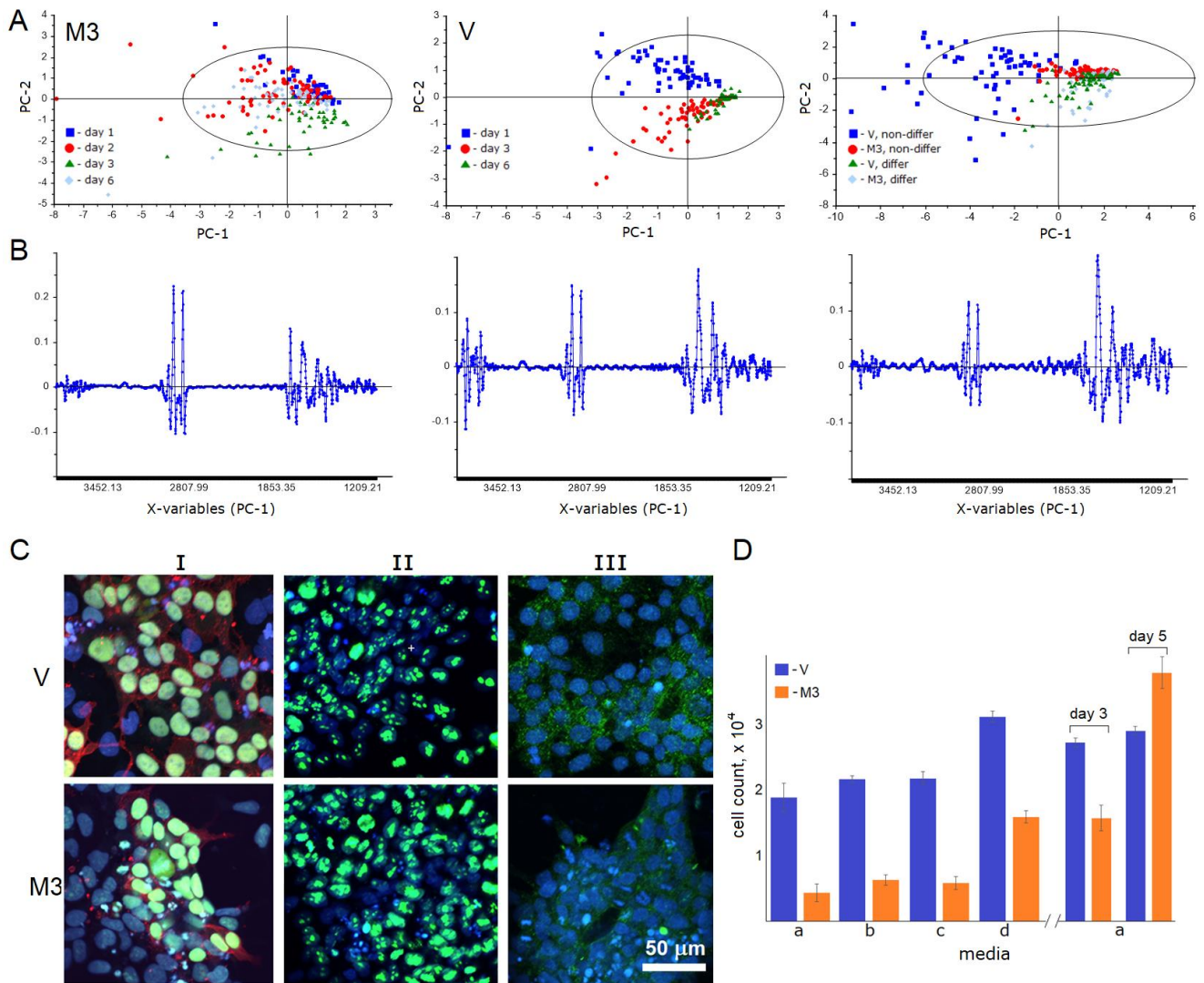


Figure 5. hESC responses under differentiating and non-differentiating conditions. (A) Score plots and (B) loading plots by PCA for the statistical analysis of hESCs grown on M3 (left) and V (middle) under differentiating conditions over time and cross-comparison of hESCs (right) grown on M3 or V over three days under differentiating and non-differentiating conditions. (C) Fluorescence micrographs of hESCs (H7.s14) grown on V and M3 over 3 days. Stain markers: Hoechst 33342 (blue) – nuclei (all); OCT4A (green) – stemness (I); SSEA3 (red) – stem cell surface (I); Ki67 (green) – proliferation (II); pFAK (green) – adhesion (III). (D) Cell count for hESCs (H14.s9) grown on M3 and V over 24 hours, 3 and 5 days in different media: (a) – Essential 8TM; (b) – mTeSRTM; (c) – mTeSRTM + cholesterol; (d) – conditioned medium.

3.5. Impact of changes in biochemical composition on cell proliferation

The lipid and protein contents of hESCs grown on M3 were not statistically different for any of the conditions and time points used and were not different from the contents of hESCs grown on V under differentiating conditions. It should be noted that cell responses resulting in differences in biochemical composition do not necessarily translate into changes in cell proliferation rates. Indeed, within different

non-differentiating conditions tested each coating supported similar proliferation rates for two types of hESCs used (Figures 5C, D, S4 & S5A). The rates were higher for the cells seeded on V than for those on M3 over the first three days of incubation but did not increase significantly thereafter (Figures 5D & S5B). The highest proliferation rates were observed for hESCs on M3 after longer incubations (Figures 5D & S5B). Interestingly, under differentiating conditions, both M3 and V promoted higher growth rates when compared to those obtained under any of non-differentiating conditions (Figure 5D & S5B). With the biochemical composition of hESCs grown on M3 being same under any conditions used, these findings indicate that the matrix or its morphology does not impact on the ability of hESCs to proliferate and does not have a substantial impact on cell proliferation rates.

4. CONCLUSIONS

Extracellular matrices are postulated to support cell development and growth, mediate cell signalling and instruct cell responses by providing niche environments. The impact of cell-matrix interactions is largely studied using physical imaging approaches, which look into changes in proliferation rates and cell morphologies including atypical features of cytoplasmic and nuclear organisation. The lack of detail in the biochemical composition of the cell at cell-matrix interfaces has stimulated the development of chemical imaging approaches, which help reveal information related to the molecular content of individual cells, and more importantly to the relative variations of the content in response to different matrices. Given that naturally occurring ECMs are protein-based materials; that is, chemically are nearly identical, matrix morphology appears as the major determinant of cell responses at cell-matrix interfaces. Notwithstanding differences in biological cues, many of which are shared between matrices of different origins, e.g., cell adhesion motifs, matrix morphologies can vary significantly, including shapes and dimensions of individual fibres, the extent of network or mesh formation.

In this study we obtained and applied hyperspectral infra-red imaging to map compositional changes of cells which were seeded and grown on a range of artificial matrices (M1-M4). These matrices exhibit similar chemistry, but lack known biological signal sequence motifs, and present distinct morphologies. To allow comparison, collagen type I (C1) and vitronectin (V) were used as a native control ECM and non-fibrous matrix protein, respectively. Both C1 and V are chemically similar to M1-M4, as they made of the same proteinogenic amino acids, but support endogenous biology such as known cell adhesion

motifs. Morphologically, C1 shares similar features with M3. The statistical analysis of hyperspectral maps showed that cells tailor their biochemical composition protein and lipid content, in response to matrix morphologies, in certain trends. Specifically, the responses of hDFs in protein content were most apparent: responses to M1 and M2 – matrices formed of non-networking fibres – were significantly different from those to C1 and M3 – matrices that do network. In the lipid content, the trend of morphological differences appeared to reflect the fibre morphology more than that of networks. Significantly different responses were found in the lipid content of cells grown on M3, M4 and C1, which exhibit heterogenous, thicker, and large fibre morphologies, and the lipid content of cells grown on M1 and M4, whose constituent fibres are thinner and shorter. The response of hESCs in the lipid and protein content to all matrices and C1 were similar or the same, but significantly different to V, which suggest that V does have a more apparent impact on cells than the matrices, likely in terms of differentiation. Amongst all matrices and C1, most significant differences between the two cell types were in the protein content for M3.

We also showed that changes in biochemical composition of the cells do not reflect their proliferation or viability properties, with matrix morphologies having no apparent effect on proliferation rates. However, ECMs proved to be indispensable for cell growth, for both human fibroblasts and human embryonic stem cells. Matrices whose morphologies were similar to those of native collagen showed similar proliferation rates with V, which is critical for the growth of embryonic stem cells. With no significant changes observed in the biochemical composition of cells grown on such matrices beyond the first day of incubation, the matrices are likely to promote or arrest the differentiation of the cells at early stages. The findings provide important insights into the chemical responses of cells to their physical extracellular environments and encourage more detailed and complementary cross-analysis with physical imaging approaches and biochemistry assays to build up the structure-function maps of cell behaviour thereby prompting the development of correlative imaging approaches. To this end, the study effectively demonstrates an information-rich methodology that can be applied for evaluating bespoke matrix materials directly at cell-matrix interfaces.

4.1. Considerations for future studies

As per the experimental design, the study focused on cell responses in 2D. Arguably, the interfacial

cell-matrix contacts are most profound in 2D and more suitable for optical and chemical imaging given the spatial resolution available. However, cell behaviour can be different in 3D environments.⁵⁰ To date, differences have been mostly shown to concern cell morphology, attachment and motility drawing upon mechanical and morphological properties of extracellular matrices. In 2D, ECMs provide stiff substrates that limit cell attachment to one plane, which results in cell multiple polarity, cell spreading and the formation of cell monolayers. These resulting features are accessible to chemical imaging. In 3D, both the cell behaviour and experimental designs for imaging are altogether different. ECMs in 3D provide soft substrates (typically as hydrogels) that encourage adhesion in a much larger space, but hinder cell spreading, polarity and monolayer formation.⁵¹ This is compounded by that cells in 3D must search and reach out to matrix fibres to create focal adhesions by forming lamellipodial extensions, which promote cell networking at different depths and planes, which is especially important for asymmetric cell organisation supporting signal synchronicity as in neurons.^{51,52} The resulting features include more heterogeneous distributions of cells per image area, which are often accompanied by spheroid formations, more round cell morphologies, appreciable cell migration and matrix re-modelling, all of which remain challenging for chemical imaging. Matrix behaviour is another factor to consider. In 2D, it concerns with how the heterogeneity of matrix coverage impacts on cell responses as variations occur in matrix morphology, e.g., M2 (Figure 1B). Given that in this study cells did not adhere without the matrices, every cell is spatially supported by the matrix. However, to define, let alone quantify, variations of matrix coverage under every cell using existing experimental setups for chemical imaging is not straightforward. Therefore, attempts to make confident conclusions over spatial variations at any level of statistical significance are deemed subject to method improvements, which favors aspirations for future studies. In 3D, the complexity increases, but also makes correlations between the behaviour of individual cells and matrix morphology more feasible, particularly with emerging 3D imaging set-ups. Regardless of the application environment, however, future studies of biochemical cell responses look into more robust developments of imaging modalities, in terms of resolution and throughput, and the implementation of data analysis approaches, including machine learning generative models, able to deconvolute and quantify the complex patterns of chemical changes in cell compositions. Recent advances already demonstrate the value of enhancing chemical imaging, e.g., mid-IR photothermal

imaging, including the application of label-free regimes and correlative approaches.^{40, 53-56} However the quantitative mapping of specific chemical changes in single cells, as opposed to comparative changes in the total protein and lipid contents, requires method improvements which can enable the identification of different classes of proteins and lipids, and their conformational states.

AUTHOR CONTRIBUTIONS

E.D.S., N.F., I.B., G.C. and M.G.R designed and supervised the research. E.D.S., N.F., C.T.R, J.E.N, I.E.K, K.H., M.T., E.M.R., M.W., M.D.F. and C.J.P performed the research. E.D.S. and M.G.R. wrote the manuscript. All authors analysed the data, contributed to the writing of the manuscript, and approved its final version.

NOTES

The authors declare no competing financial interests.

Supporting Information. Additional spectral maps, FT-IR spectra and PCA plots of cells at cell-matrix interfaces; electron and atomic force micrographs of individual cells highlighting cell morphology and matrix fibers; fluorescence micrographs of hESCs grown under various differentiating and non-differentiating conditions.

ACKNOWLEDGEMENTS

We acknowledge funding from the UK's Department for Business, Energy and Industrial Strategy, from the UK Research and Innovation (Medical Research Council; No. MR/X000028/1) and from the UK Regenerative Medicine Platform (No: MR/R015724/1).

REFERENCES

1. Holmes, D. F.; Yeung, C. C.; Garva, R.; Zindy, E.; Taylor, S. H.; Lu, Y.; Watson, S.; Kalson, N. S.; Kadler, K. E. Synchronized Mechanical Oscillations at the Cell-Matrix Interface in the Formation of Tensile Tissue. *Proc. Natl. Acad. Sci. USA* **2018**, *115*, E9288-E9297.
2. Ohta, Y.; Fujii, M.; Takahashi, S.; Takano, A.; Nanki, K.; Matano, M.; Hanyu, H.; Saito, M.; Shimokawa, M.; Nishikori, S.; Hatano, Y.; Ishii, R.; Sawada, K.; Machinaga, A.; Ikeda, W.; Imamura, T.; Sato T. Cell-Matrix Interface Regulates Dormancy in Human Colon Cancer Stem Cells. *Nature* **2022**, *608*, 784-794.

3. Moretti, L.; Stalfort, J.; Barker, T. H.; Abebayehu, D. The Interplay of Fibroblasts, the Extracellular Matrix, and Inflammation in Scar Formation. *J. Biol. Chem.* **2022**, *298*, 101530.
4. Sahl, S. J.; Hell, S. W.; Jakobs, S. Fluorescence Nanoscopy in Cell Biology. *Nat. Rev. Mol. Cell. Biol.* **2017**, *18*, 685-701.
5. Heinrich, L.; Bennett, D.; Ackerman, D.; Park, W.; Bogovic, J.; Eckstein, N.; Petrucio, A.; Clements, J.; Pang, S.; Xu, C. S.; Funke, J.; Korff, W.; Hess, H. F.; Lippincott-Schwartz, J.; Saalfeld, S.; Weigel, A. V.; COSEM Project Team. Whole-Cell Organelle Segmentation in Volume Electron Microscopy. *Nature* **2021**, *599*, 141-146.
6. Dufrêne, Y. F.; Ando, T.; Garcia, R.; Alsteens, D.; Martinez-Martin, D.; Engel, A.; Gerber, C.; Müller, D. J. Imaging Modes of Atomic Force Microscopy for Application in Molecular and Cell Biology. *Nat. Nanotechnol.* **2017**, *12*, 295-307.
7. Jiang, H.; Favaro, E.; Goulbourne, C. N.; Rakowska, P. D.; Hughes, G. M.; Ryadnov, M. G.; Fong, L. G.; Young, S. G.; Ferguson, D. J.; Harris, A. L.; Grovenor C. R. Stable Isotope Imaging of Biological Samples with High Resolution Secondary Ion Mass Spectrometry and Complementary Techniques. *Methods* **2014**, *68*, 317-324.
8. Passarelli, M. K.; Pirkl, A.; Moellers, R.; Grinfeld, D.; Kollmer, F.; Havelund, R.; Newman, C. F.; Marshall, P. S.; Arlinghaus, H.; Alexander, M. R.; West, A.; Horning, S.; Niehuis, E.; Makarov, A.; Dollery, C. T.; Gilmore, I. S. The 3D OrbiSIMS-Label-Free Metabolic Imaging with Subcellular Lateral Resolution and High Mass-Resolving Power. *Nat. Methods* **2017**, *14*, 1175-1183.
9. Narayan, K.; Prosa, T. J.; Fu, J.; Kelly, T. F.; Subramaniam, S. Chemical Mapping of Mammalian Cells by Atom Probe Tomography. *J. Struct. Biol.* **2012** *178*, 98-107.
10. Jamin, N.; Dumas, P.; Moncuit, J.; Fridman, W-H.; Teillaud, J.-L.; Carr, G. L.; Williams, G. P. Highly Resolved Chemical Imaging of Living Cells by Using Synchrotron Infrared Microspectrometry. *Proc. Natl. Acad. Sci.* **1998**, *95*, 4837-4840.
11. Palonpon, A. F.; Ando, J.; Yamakoshi, H.; Dodo, K.; Sodeoka, M.; Kawata, S.; Fujita, K. Raman and SERS Microscopy for Molecular Imaging of Live Cells. *Nat. Protoc.* **2013**, *8*, 677-692.

12. Živanović, V.; Semini, G.; Laue, M.; Drescher, D.; Aebischer, T.; Kneipp, J. Chemical Mapping of Leishmania Infection in Live Cells by SERS Microscopy. *Anal. Chem.* **2018**, *90*, 8154-8161.
13. Rakowska, P. D.; Jiang, H.; Ray, S.; Pyne, A.; Lamarre, B.; Carr, M.; Judge, P. J.; Ravi, J.; Gerling, U. I.; Kokscha, B.; Martyna, G. J.; Hoogenboom, B. W.; Watts, A.; Crain, J.; Grovenor, C. R.; Ryadnov, M. G. Nanoscale Imaging Reveals Laterally Expanding Antimicrobial Pores in Lipid Bilayers. *Proc. Natl. Acad. Sci. USA* **2013**, *110*, 8918-8923.
14. Matthäus, C.; Bird, B.; Miljković, M.; Chernenko, T.; Romeo, M.; Diem, M. Infrared and Raman Microscopy in Cell Biology. *Methods Cell Biol.* **2008** *89*, 275-308.
15. Tsikritsis, D.; Shi, H.; Wang, Y.; Velugotla, S.; Sršen, V.; Elfick, A.; Downes A. Label-Free Biomarkers of Human Embryonic Stem Cell Differentiation to Hepatocytes. *Cytometry A.* **2016**, *89*, 575-584.
16. Aksoy, C.; Severcan, F. Infrared Spectroscopy and Imaging in Stem Cells and Aging Research. *Methods Mol. Biol.* **2019**, *2045*, 201-221.
17. Quaroni, L.; Zlateva, T.; Wehbe, K.; Cinque, G. Infrared Imaging of Small Molecules in Living Cells: From *In Vitro* Metabolic Analysis to Cytopathology. *Faraday Discuss.* **2016**, *187*, 259-271.
18. Pleitez, M. A.; Khan, A. A.; Soldà, A.; Chmyrov, A.; Reber, J.; Gasparin, F.; Seeger, M. R.; Schätz, B.; Herzig, S.; Scheideler, M.; Ntziachristos, V. Label-Free Metabolic Imaging by Mid-Infrared Optoacoustic Microscopy in Living Cells. *Nat. Biotechnol.* **2020**, *38*, 293-296.
19. Mourant, J. R.; Short, K. W.; Carpenter, S.; Kunapareddy, N.; Coburn, L.; Powers, T. M.; Freyer, J. P. Biochemical Differences in Tumorigenic and Nontumorigenic Cells Measured by Raman and Infrared Spectroscopy. *J. Biomed. Opt.* **2005**, *10*, 031106.
20. Mourant, J. R.; Yamada, Y. R.; Carpenter, S.; Dominique, L. R.; Freyer, J. P. FTIR Spectroscopy Demonstrates Biochemical Differences in Mammalian Cell Cultures at Different Growth Stages. *Biophys. J.* **2003** *85*, 1938-1947.
21. Cai, L.; Heilshorn, S. C. Designing ECM-Mimetic Materials Using Protein Engineering. *Acta Biomater.* **2014**, *10*, 1751-1760.

22. Bella, A.; Ray, S.; Shaw, M.; Ryadnov, M. G. Arbitrary Self-Assembly of Peptide Extracellular Microscopic Matrices. *Angew. Chem. Int. Ed. Engl.* **2012**, *51*, 428-431.
23. Faruqui, N.; Bella, A.; Ravi, J.; Ray, S.; Lamarre, B.; Ryadnov, M. G. Differentially Instructive Extracellular Protein Micro-Nets. *J. Am. Chem. Soc.* **2014**, *136*, 7889-7898.
24. De Santis, E.; Faruqui, N.; Noble, J. E.; Ryadnov, M. G. Exploitable Length Correlations in Peptide Nanofibres. *Nanoscale* **2014**, *6*, 11425-11430.
25. Ravi, J.; Bella, A.; Correia, A. J.; Lamarre, B.; Ryadnov, M. G. Supramolecular Amphipathicity for Probing Antimicrobial Propensity of Host Defence Peptides. *Phys. Chem. Chem. Phys.* **2015**, *17*, 15608-15614.
26. Cinque, G.; Frogley, M.; Wehbe, K.; Filik, J.; Pijanka, J. Multimode Infrared Imaging and Microspectroscopy (MIRIAM) Beamline at Diamond. *Synchrotron Radiat. News* **2011**, *24*, 24–33.
27. Azizian Kalkhoran M, Douglas Winter A, Cinque G. Beamshaping for Infrared Hyperspectral Imaging: A Sequential Optimization for InfraRed Source Coupling. *Opt. Lett.* **2022**, *47*, 2959-2962.
28. Thomson, J.A.; Itskovitz-Eldor, J.; Shapiro, S. S.; Waknitz, M. A.; Swiergiel, J. J.; Marshall, V. S.; Jones, J. M. Embryonic Stem Cell Lines Derived from Human Blastocysts. *Science* **1998**, *282*, 1145–1147.
29. Draper, J.; Smith, K.; Gokhale, P.; Moore, H. D.; Maltby, E.; Johnson, J.; Meisner, L.; Zwaka, T. P.; Thomson, J. A.; Andrews, P. W. Recurrent Gain of Chromosomes 17q and 12 in Cultured Human Embryonic Stem Cells. *Nat. Biotechnol.* **2004**, *22*, 53–54.
30. Donaldson, P. M.; Kelley, C. S.; Frogley, M. D.; Filik, J.; Wehbe, K.; Cinque, G. Broadband Near-Field Infrared Spectromicroscopy Using Photothermal Probes and Synchrotron Radiation. *Opt. Express* **2016**, *24*, 1852-1864.
31. Wang, Y.; Dai, W.; Liu, Z.; Liu, J.; Cheng, J.; Li, Y.; Li, X.; Hu, J.; Lü, J. Single-Cell Infrared Microspectroscopy Quantifies Dynamic Heterogeneity of Mesenchymal Stem Cells During Adipogenic Differentiation. *Anal. Chem.* **2021**, *93*, 671-676.

32. Lasalvia, M.; Capozzi, V.; Perna, G. Comparison of FTIR Spectra of Different Breast Cell Lines to Detect Spectral Biomarkers of Pathology. *Infrared Phys. Technol.* **2022**, *120*, 103976.
33. Quaroni L, Zlateva T. Infrared Spectromicroscopy of Biochemistry in Functional Single Cells. *Analyst* **2011**, *136*, 3219–3232.
34. Kenkel, S.; Gryka, M.; Chen, L.; Confer, M. P.; Rao, A.; Robinson, S.; Prasanth, K. V.; Bhargava, R. Chemical Imaging of Cellular Ultrastructure by Null-Deflection Infrared Spectroscopic Measurements. *Proc. Natl. Acad. Sci. USA* **2022**, *119*, e2210516119.
35. Kenkel, S.; Mittal, S.; Bhargava, R. Closed-Loop Atomic Force Microscopy-Infrared Spectroscopic Imaging for Nanoscale Molecular Characterization. *Nat. Commun.* **2020**, *11*, 3225.
36. Clemens, G.; Flower, K. R.; Henderson, A. P.; Whiting, A.; Przyborski, S. A.; Jimenez-Hernandez, M.; Ball, F.; Bassan, P.; Cinque, G.; Gardner, P. The Action of All-Trans-Retinoic Acid (ATRA) and Synthetic Retinoid Analogues (EC19 and EC23) on Human Pluripotent Stem Cells Differentiation Investigated Using Single Cell Infrared Microspectroscopy. *Mol. Biosyst.* **2013**, *9*, 677-692.
37. Hughes, C.; Henderson, A.; Kansiz, M.; Dorling, K. M.; Jimenez-Hernandez, M.; Brown, M. D.; Clarke, N. W.; Gardner, P. Enhanced FTIR Bench-Top Imaging of Single Biological Cells. *Analyst* **2015**, *140*, 2080-2085.
38. Gelfand, P.; Smith, R. J.; Stavitski, E.; Borchelt, D. R.; Miller, L. M. Characterization of Protein Structural Changes in Living Cells Using Time-Lapsed FTIR Imaging. *Anal. Chem.* **2015**, *87*, 6025–6031.
39. Chan, K. L. A.; Fale, P. L.V.; Atharawi, A.; Wehbe, K.; Cinque, G. Subcellular Mapping of Living Cells Via Synchrotron MicroFTIR and ZnS Hemispheres. *Anal. Bioanal. Chem.* **2018**, *410*, 6477-6487.
40. Chan, K. L. A.; Lekkas, I.; Frogley, M. D.; Cinque, G.; Altharawi, A.; Bello, G.; Dailey, L. A. Synchrotron Photothermal Infrared Nanospectroscopy of Drug-Induced Phospholipidosis in Macrophages. *Anal. Chem.* **2020**, *92*, 8097-8107.

41. Dumas, P.; Sockalingum, G. D.; Sule-Suso, J. Adding Synchrotron Radiation to Infrared Microspectroscopy: What's New in Biomedical Applications? *Trends Biotechnol.* **2007**, *25*, 40–44.
42. Tobin, M. J.; Puskar, L.; Barber, R. L.; Harvey, E. C.; Heraud, P.; Wood, B. R.; Bambery, K. R.; Dillon, C. T.; Munro, K. L. FTIR Spectroscopy of Single Live Cells in Aqueous Media by Synchrotron IR Microscopy Using Microfabricated Sample Holders. *Vib. Spectrosc.* **2010**, *53*, 34–38.
43. Yao, S.; Moenner, M.; Engdahl, A.; Petibois, C. Use of Synchrotron-Radiation-Based FTIR Imaging for Characterizing Changes in Cell Contents. *Anal. Bioanal. Chem.* **2012**, *404*, 1311-1316.
44. Fisher, G. J.; Varani, J.; Voorhees, J. J. Looking Older: Fibroblast Collapse and Therapeutic Implications. *Arch. Dermatol.* **2008**, *144*, 666-672.
45. Hilton, S. A.; Dewberry, L. C.; Hodges, M. M.; Hu, J.; Xu, J.; Liechty, K. W.; Zgheib, C. Mesenchymal Stromal Cells Contract Collagen More Efficiently than Dermal Fibroblasts: Implications for Cytotherapy. *PLoS One* **2019**, *14*, e0218536.
46. Zajiczek, L.; Shaw, M.; Faruqui, N.; Bella, A.; Pawar, V. M.; Srinivasan, M. A.; Ryadnov, M. G. Nano-Mechanical Single-Cell Sensing of Cell-Matrix Contacts. *Nanoscale* **2016**, *8*, 18105-18112.
47. Heydarkhan-Hagvall, S.; Gluck, J. M.; Delman, C.; Jung, M.; Ehsani, N.; Full, S.; Shemin, R. J. The Effect of Vitronectin on the Differentiation of Embryonic Stem Cells in a 3D Culture System. *Biomaterials* **2012**, *33*, 2032-2240.
48. Ami, D.; Neri, T.; Natalello, A.; Mereghetti, P.; Doglia, S. M.; Zanoni, M.; Zuccotti, M.; Garagna, S.; Redi, C. A. Embryonic Stem Cell Differentiation Studied by FT-IR Spectroscopy. *Biochim. Biophys. Acta.* **2008**, *1783*, 98-106.
49. Mata-Miranda M. M.; Vazquez-Zapien, G. J.; Rojas-Lopez, M.; Sanchez-Monroy, V.; Perez-Ishiwara, D. G., Delgado-Macuil, R. J. Morphological, Molecular and FTIR Spectroscopic Analysis during the Differentiation of Kidney Cells from Pluripotent Stem Cells. *Biol. Res.* **2017**, *50*, 14.

50. Discher, D. E.; Mooney, D. J.; Zandstra, P. W. Growth Factors, Matrices, and Forces Combine and Control Stem Cells. *Science* **2009**, *324*, 1673-1677.
51. Faruqi, N.; Williams, D. S.; Briones, A.; Kepiro, I. E.; Ravi, J.; Kwan, T. O. C.; Mearns-Spragg, A.; Ryadnov, M. G. Extracellular Matrix Type 0: From Ancient Collagen Lineage to a Versatile Product Pipeline – JellaGel™. *Mater. Today Bio.* **2023**, *22*, 100786.
52. Lim, J. M.; Park, C.; Park, J. S.; Kim, C.; Chon, B.; Cho, M. Cytoplasmic Protein Imaging with Mid-Infrared Photothermal Microscopy: Cellular Dynamics of Live Neurons and Oligodendrocytes. *J. Phys. Chem. Lett.* **2019**, *10*, 2857-2861.
53. Ishigane, G.; Toda, K.; Tamamitsu, M.; Shimada, H.; Badarla, V. R.; Ideguchi, T. Label-Free Mid-Infrared Photothermal Live-Cell Imaging Beyond Video Rate. *Light Sci. Appl.* **2023**, *12*, 174.
54. Zhang, Y.; Zong, H.; Zong, C.; Tan, Y.; Zhang, M.; Zhan, Y.; Cheng, J. X. Fluorescence-Detected Mid-Infrared Photothermal Microscopy. *J. Am. Chem. Soc.* **2021**, *143*, 11490-11499.
55. Kontsek, E.; Pesti, A.; Björnstedt, M.; Üveges, T.; Szabó, E.; Garay, T.; Gordon P, Gergely S, Kiss A. Mid-Infrared Imaging Is Able to Characterize and Separate Cancer Cell Lines. *Pathol. Oncol. Res.* **2020**, *26*, 2401-2407.
56. Yamada, K. M.; Doyle, A. D.; Lu, J. Cell-3D Matrix Interactions: Recent Advances and Opportunities. *Trends Cell Biol.* **2022**, *32*, 883-895.